

# Forced Enhanced Atomic Refinement Modeling of the Metallic Glass $\text{Cu}_{46}\text{Zr}_{46}\text{Al}_8$

Rajendra Thapa,\* Kashi Nath Subedi, Bishal Bhattarai, and David A. Drabold

Herein, the structure of  $\text{Cu}_{46}\text{Zr}_{46}\text{Al}_8$  is inverted from X-ray structure factor data and energy minimizations as implemented with forced enhanced atomic refinement (FEAR). The models generated are in good agreement with structural data obtained from diffraction experiment. Voronoi tessellation analysis shows reasonable agreement with previous results, and the models include structural units believed to have slow dynamics near glass transition and be responsible for the excellent glass forming ability of this metallic glass. It is shown, with constant temperature molecular dynamics (MD), that there is a significant increase in the fraction of these particular clusters near the glass transition. Space-projected conductivity (SPC) calculations show that conduction through Zr dominates over Cu. Vibrational modes are strongly localized on a few Al atoms at high frequencies and distributed almost uniformly on Cu and Zr atoms at low frequencies.

Al atoms. The Zr–Al bonding is also demonstrated by nuclear magnetic resonance (NMR) studies by Xi et al.<sup>[13]</sup> Both extended X-ray absorption spectra (EXAFS)<sup>[10]</sup> and X-ray diffraction studies<sup>[11,12]</sup> have shown that the addition of Al to Cu–Zr BMG increases the fraction of icosahedron such as clusters and makes the distribution of Al homogeneous, which enhances the GFA by increasing the structural incompatibility with the crystalline phases. X-ray diffraction pattern from samples with varying Al concentration has showed that even at 4% Al concentration, a fully amorphous rod up to 5 mm in size can be produced.<sup>[17]</sup> Yu et al.<sup>[17]</sup> also found that the critical cooling rate for Cu–Zr BMG drops from 250 to 40 K s<sup>-1</sup> with just 4% Al doping.

## 1. Introduction

Bulk metallic glasses (BMGs) form a family of one of the most researched amorphous materials. The ever growing scientific attention can be attributed to their unique properties, such as ultrahigh strength, resistance to wear and corrosion,<sup>[1]</sup> etc. Such properties enable its diverse applicability, ranging from sporting goods to nanotechnology and biomedical applications.<sup>[2]</sup> Despite having numerous models for structure,<sup>[3–6]</sup> glass forming ability (GFA),<sup>[7]</sup> and its relation to the structure, a plethora of basic questions still remains unanswered. Cu–Zr BMG gained particular interest after its discovery challenged the pre-existing understanding of GFA.<sup>[8]</sup> For these reasons, Cu–Zr–Al forms one of the most highly researched materials in the BMG family with both experimental<sup>[9–13]</sup> and theoretical work<sup>[14–16]</sup> being reported. Georarakis et al.,<sup>[9]</sup> with his X-ray pair distribution function (PDF) experiments, showed that the addition of Al to Cu–Zr BMG induces changes in the atomic structure in the short and medium range order, attributed to the strong bonding preference between Zr and

Molecular dynamics (MD) simulations by Zhang et al.<sup>[16]</sup> have also revealed superior GFA in  $\text{Cu}_{46}\text{Zr}_{46}\text{Al}_8$  relative to other compositions, in agreement with experiment.<sup>[11,12]</sup> Structure inversion with reverse Monte Carlo (RMC) of Cu–Zr–Al BMGs from experimental information has already been carried out with large number of atoms.<sup>[11,12,18]</sup> However, traditional RMC alone may produce non-physical solutions even for elemental systems.<sup>[19]</sup> In this work, we report on models designed to closely agree with experiment and, at the same time, be a suitable minimum of a standard density functional theory (DFT) code.

The rest of this article is organized as follows: Section 2 has discussions about computational methodology and model generation using forced enhanced atomic refinement (FEAR) and melt quench (MQ). Section 3 deals with results obtained from structural, electronic, and vibrational calculations, and Section 4 summarizes our conclusions.

## 2. Methodology and Models

In this study, we perform an ab initio simulation of  $\text{Cu}_{46}\text{Zr}_{46}\text{Al}_8$  to determine the structural and electronic properties using the FEAR<sup>[20–23]</sup> technique and a traditional MQ method. FEAR has shown promise in modeling a wide range of amorphous systems, ranging from a-Si,<sup>[24]</sup> a-SiO<sub>2</sub>, silver-doped GeSe<sub>3</sub>, sodium silicate glass,<sup>[25]</sup> and a-C<sup>[23,26]</sup> to complex BMGs.<sup>[27]</sup>

FEAR aims to use experimental information to aid and accelerate ab initio simulation of disordered materials. Of course, diffraction data by itself are grossly inadequate to determine the structure of a complex system with rich local chemical and topological order. However, when chemical information is included (from an accurate quantum mechanical code), we have

R. Thapa, K. N. Subedi, Prof. D. A. Drabold  
Department of Physics and Astronomy  
Ohio University  
Athens, OH 45701, USA  
E-mail: rt887917@ohio.edu

Dr. B. Bhattarai  
Department of Physics  
Missouri University of Science and Technology  
Rolla, MO 65409, USA

 The ORCID identification number(s) for the author(s) of this article can be found under <https://doi.org/10.1002/pssb.202000415>.

DOI: 10.1002/pssb.202000415

repeatedly shown that FEAR produces models equal or superior to MQ, even in total energy, and requires a fraction of the (expensive) force calls needed by MQ methods.

To provide some more detail, we start with some definitions. If  $V$  is an energy functional and  $\chi^2$  gauges the discrepancy between a diffraction experiment and a computer model, we seek to find a set of atomic coordinates that renders  $V$  a minimum, and  $\chi^2$  within experimental error. FEAR is a simple iterative process consisting of 1) producing a structural model with random coordinates and 2) invoking  $N$  accepted moves within conventional RMC followed by  $M$  conjugate-gradient (CG) steps using ab initio interactions. We then iterate 2) until convergence. The final results do not depend heavily on the numerical values of  $N$  and  $M$ , which were chosen to be 150 and 5, respectively, for the present work. FEAR avoids the problem of the relative weighting of  $V$  and  $\chi^2$  in a penalty or target energy functional as in hybrid approaches. If the density of the material is unknown, it is possible to run the simulation at zero pressure (with variable cell geometries) in the CG loop and simply pass the modified supercell vectors back to the RMC loop.

### 2.1. FEAR-I

A FEAR model of  $\text{Cu}_{46}\text{Zr}_{46}\text{Al}_8$  was made with 300 atoms in a box of size 17.0805 Å corresponding to an experimental density of  $7.38 \text{ g cc}^{-1}$ .<sup>[12]</sup> A sequence of partial RMC fitting using RMCProfile<sup>[28]</sup> and partial energy minimizations, using Vienna ab initio simulation package (VASP),<sup>[29–31]</sup> complemented each other and were iterated until convergence (when the structure factor of the model was close to experiment and the forces were near zero at a suitable potential energy minimum). We used the experimental data of the previous study<sup>[12]</sup> and the code RMCProfile. Our total energy/force code is the ab initio plane-wave DFT package VASP. After convergence, the converged structure is then fully relaxed with VASP until the forces on each atom drop to below  $0.005 \text{ eV \AA}^{-1}$ . The maximum move for each atomic species during the RMC refinement was kept at 0.085 Å. Energy minimization steps in VASP with a plane wave basis set and a projector-augmented wave (PAW) method<sup>[32,33]</sup> with Perdew–Burke–Ernzerhof (PBE) functional.<sup>[34]</sup> The final relaxation step used VASP for  $\Gamma(k=0)$ , a plane-wave cutoff of 280 eV and an energy convergence tolerance of  $10^{-5} \text{ eV}$ . A total of 400 FEAR steps were used to reach the desired convergence.

The computational cost for this model was  $\approx 1866$  core hours at BRIDGES at Pittsburgh Supercomputer Center.

### 2.2. FEAR-II

This model was made with exactly the same implementation as FEAR-I but starts from a different initial configuration: the atomic positions of a well-equilibrated liquid melt at 1500 K were taken as the starting model.

### 2.3. Melt Quench

For the purpose of comparison and cross validation of the models created, we also prepared an MQ model, starting with the same

random coordinates used in FEAR-I, using VASP. The model was heated to 1500 K, equilibrated at 1500 K, cooled to 1000 K, equilibrated at 1000 K, cooled to 300 K, and finally equilibrated at 300 K. This equilibrated model is finally relaxed using the CG method until the forces on each atom drop to below  $0.005 \text{ eV \AA}^{-1}$ . Throughout the simulation, a time step of 2.0 fs was adopted, and the total simulation time was 45 ps for a computational time of 11 000 core hours on the same machine as model FEAR-I.

To keep it simple and consistent, we follow the same “color nomenclature” for the atomic species: red for Zr, green for Cu, and blue for Al in the figures.

## 3. Results and Discussion

### 3.1. Structural Properties

In **Figure 1**, we show the final relaxed atomic structure of the FEAR-I. Atoms are packed in continuous random arrangement, the dense composition being responsible for a high coordination number. The distribution of Al seems reasonably homogeneous, with no clustering, and is believed to be responsible for suppressing crystallization and thereby increasing the GFA.<sup>[10–12]</sup>

The structure factor and pair distribution function of the models are shown in **Figure 2**. The left panel displays a comparison of  $S(q)$  between the experiment<sup>[12]</sup> and the models, showing good agreement. On the right panel, PDF  $G(r)$  is similarly compared. Broad peaks in the PDF of the models suggest the amorphous nature of the material. The first minimum of the PDF obtained from the models matches with the experiment suggesting a good agreement in short-range order. The first peak arises from joint contributions from all six partial PDFs (**Figure 3**).

To study the bonding preferences of the atomic species involved, we calculated the number of nearest neighbors around each atom using a cutoff radius of 3.5 Å, and the details of are given in **Table 1**. The table suggests that Al bonds preferentially

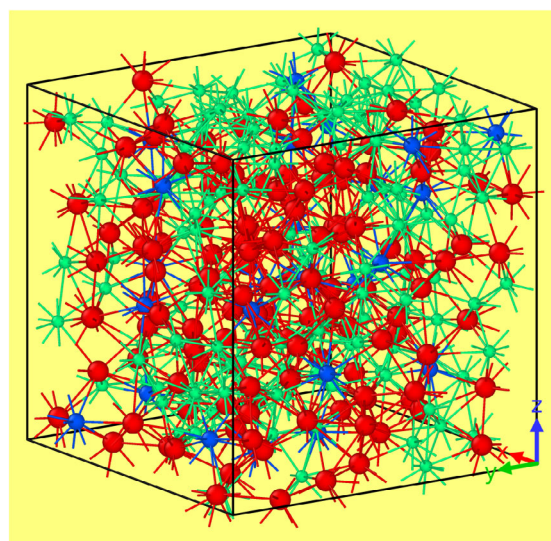


**Figure 1.** Simulated atomic structure obtained for FEAR-I. Zr, Cu, and Al atoms are shown in red, green, and blue, respectively, and the same “color nomenclature” will be used in all figures.

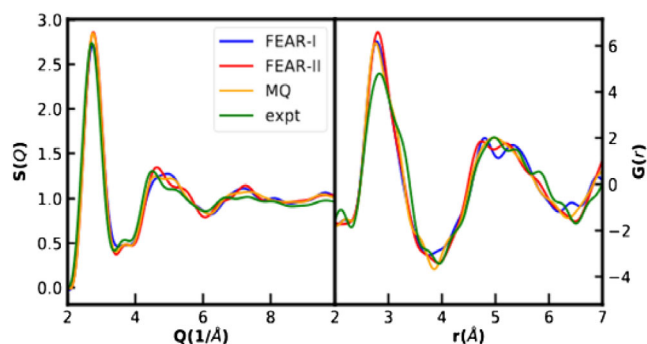


**Figure 2.** Comparison of structure factor and pair distribution function obtained from models with experiment.

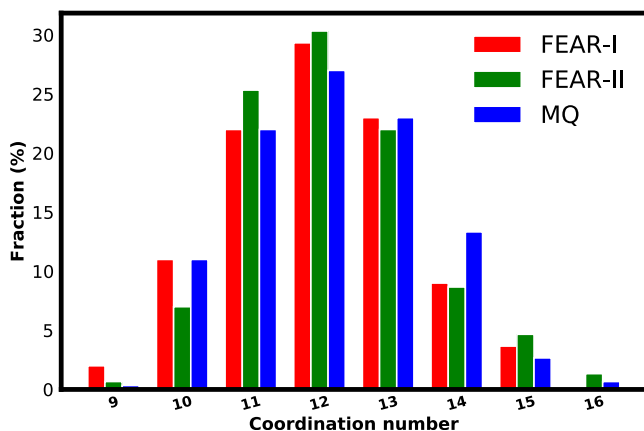


**Figure 3.** Fraction of different coordination numbers present in the samples. The coordination number is peaked around 12, suggesting dominance of icosahedron structures.

**Table 1.** Coordination statistics: average coordination number and its distribution of constituent atoms.

	Atom	$n$	$n(\text{Zr})$	$n(\text{Cu})$	$n(\text{Al})$
FEAR-I	Zr	12.86	5.91	5.80	1.15
	Al	11.79	6.63	5.08	0.08
	Cu	11.22	5.80	4.54	0.88
FEAR-II	Zr	13.10	5.81	6.12	1.17
	Al	11.83	6.70	4.96	0.17
	Cu	11.30	6.12	4.32	0.86
MQ	Zr	13.07	5.78	6.08	1.21
	Al	12.12	6.96	4.92	0.25
	Cu	11.24	6.08	4.30	0.86

with Zr over Cu in agreement with previously reported strong interaction between Zr and Al atoms.<sup>[9]</sup>

### 3.2. Voronoi Analysis

The nearest neighbor environment of the atoms was studied using the poly-disperse Voronoi tessellation, as implemented

in the OVITO software,<sup>[35]</sup> with the Goldschmidt radius (1.60 Å for Zr, 1.43 Å for Al, and 1.28 Å for Cu). The Voronoi cell of an atom is the region of real space closer to that particle than any other.<sup>[36]</sup> Details about the Voronoi polyhedra can be found elsewhere.<sup>[36]</sup> In general, a Voronoi polyhedron (VP) for an atom can be manually constructed by connecting perpendicular bisector planes between that atom and all its nearest neighbors. The 3D geometry thus obtained is characterized with indexes written in the form  $\langle n_3 n_4 n_5 n_6 \rangle$ , where  $n_i$  denotes the number of faces with  $i$  edges present in the VP. The distribution of prominent Voronoi polyhedra is shown in **Figure 4**. A polyhedron is called prominent if it makes up more than 3% of the total number of polyhedra. For Zr atoms, most of the dominant polyhedra are not perfect icosahedra (ICO) ( $\langle 00120 \rangle$ ) but ICO-like with Voronoi indices  $\langle 0285 \rangle$ ,  $\langle 0286 \rangle$ ,  $\langle 01104 \rangle$ , etc. However, there are ideal ICO clusters in the network centered at Cu and Al atoms. These cluster statistics are in good agreement with results from the previous study.<sup>[16]</sup>

The Cu-centered  $\langle 00120 \rangle$ ,  $\langle 0282 \rangle$  and Zr-centered  $\langle 01104 \rangle$  are believed to have the slowest dynamics in Cu–Zr liquids<sup>[37,38]</sup> and are associated with the excellent GFA. These polyhedra also make up a significant fraction of the Voronoi polyhedra in our models. To study the fluctuations of the fraction of these clusters with temperature, together with other dominant VPs, we perform a constant temperature MD simulation of the MQ model at several different temperatures. The results, averaged over 500 configurations (the last ps of the MD simulation), are shown in **Figure 5**. In the vicinity of the glass transition temperature for  $\text{Cu}_{46}\text{Zr}_{46}\text{Al}_8$  ( $\approx 700$  K), our models show a significant increase in the fraction of clusters that are believed to have slow dynamics,<sup>[37,38]</sup> which explains the high GFA associated with this stoichiometry. There is a gradual increase in the fraction of  $\langle 0281 \rangle$  VP, making it the most common VP in the MQ model, in agreement with Wang et al.<sup>[12]</sup>

In addition to the ideal ICO, the Cu atoms have ICO-like ( $\langle 0282 \rangle$ ,  $\langle 0364 \rangle$ ,  $\langle 0281 \rangle$ ) clusters in large numbers. If we look at the system as a whole, it is obvious that ideal ICO are not the most dominant structure, again in agreement with Wang et al.<sup>[12]</sup>

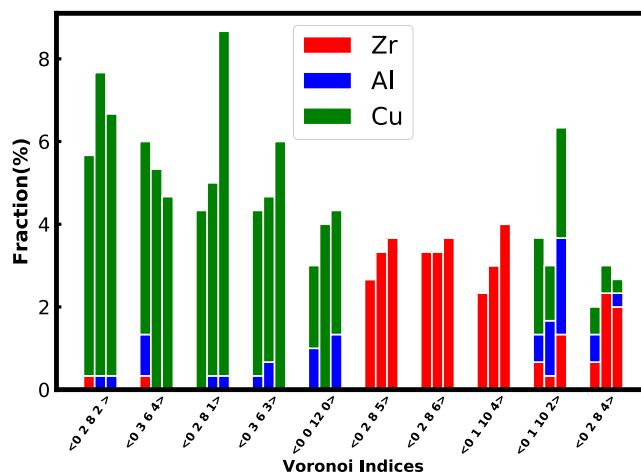


**Figure 4.** Concentration (in %) of the dominant polyhedra. The left bars on each Voronoi index correspond to FEAR-I, middle bar to FEAR-II, and the right to MQ models.

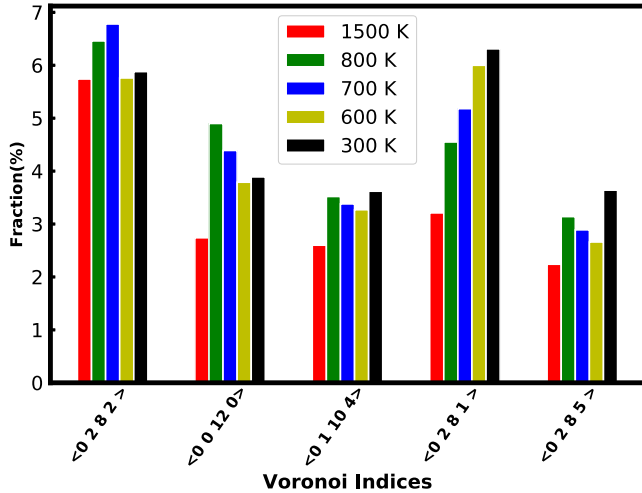


**Figure 5.** Temperature dependence of the fraction of slow dynamics clusters. A gradual increase in the concentration of  $\langle 0281 \rangle$  Voronoi polyhedra with the decrease in temperature is seen.

### 3.3. Electronic Properties

The electronic structure of the models was studied using total density of states (DoS), partial DoS, and inverse participation ratio (IPR). The DoS for FEAR-I is very similar to other models and is shown in **Figure 6**. The Fermi level corresponds to the zero of the energy scale marked by vertical drop lines. Significant contributions to the total DoS arise from the hybridization of

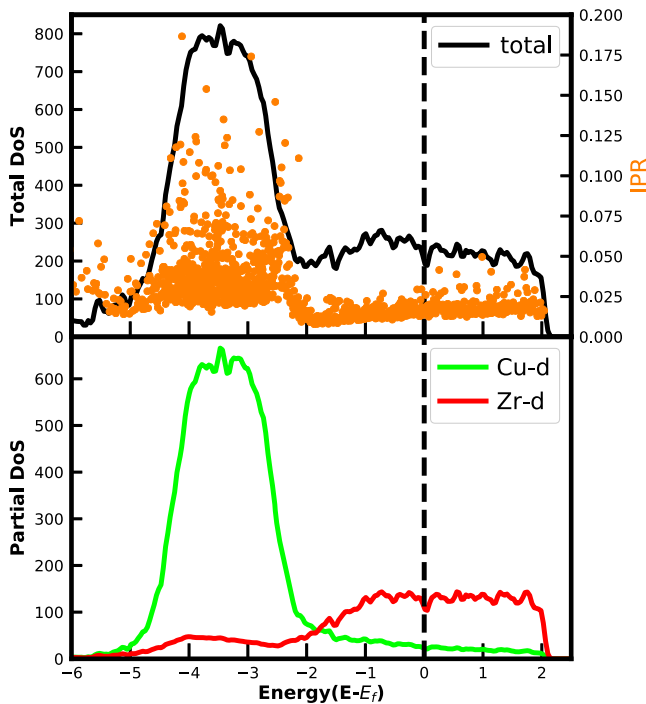


**Figure 6.** Electronic DoS of the FEAR-I model. The localization of the states is shown with IPR. Partial DoS that contributes most significantly to the DoS near the Fermi level is shown in the bottom panel.

the d-orbitals of Cu and Zr, whereas the contribution of Al remains nominal. Existence of states in the vicinity of the Fermi level suggests conducting behavior of the samples. The contribution from Zr atoms, however, is much higher than that of Cu near the Fermi level, and a result is also seen in Hall coefficient measurements of the Cu–Zr–Al system.<sup>[39]</sup> Similar electronic analysis on  $\text{Cu}_{50}\text{Zr}_{50}$ <sup>[40]</sup> showed qualitatively the same results, which suggest that 8% Al doping does not significantly impact electronic properties. Details of the more active conduction parts of the network will be discussed in the next section.

The localization of Kohn–Sham states is given by IPR defined as

$$\mathcal{I}(\psi_n) = \frac{\sum_i |a_n^i|^4}{(\sum_i |a_n^i|^2)^2} \quad (1)$$

where  $a_n^i$  is the contribution to the eigenvector  $\psi_n$  from the  $i$ th atomic orbital (s, p, and d) as calculated with VASP. In simple terms, localized states have high IPR value (ideally equal to  $\mathcal{I} = 1$ ), whereas a completely extended state produces a value of  $(1/N)$ , i.e., evenly distributed over  $N$  atoms. Close to the Fermi level, we observe low IPR indicating delocalized states and conducting behavior of the models.

#### 3.3.1. Space-Projected Conductivity

The information given by DoS about the species decomposed contribution near the Fermi level is not a full treatment of conduction activity within the network, because the conduction also depends on the localization of the electronic states and momentum matrix elements between Kohn–Sham states near the Fermi level. Recently, we have developed a technique to visualize conductivity in real space by undertaking a spatial decomposition of the Kubo–Greenwood<sup>[41,42]</sup> formula. We start by defining a discrete grid in real space and show that the quantity

$$\zeta(\mathbf{x}) = \left| \sum_{\mathbf{x}'} \Gamma(\mathbf{x}, \mathbf{x}') \right| \quad (2)$$

may be interpreted as a space-projected conductivity (SPC), providing information about what parts of the network are contributing to electronic conduction. Here,  $\mathbf{x}$  is a grid point, and we introduce

$$\Gamma(\mathbf{x}, \mathbf{x}') = \sum_{ij\alpha} g_{ij}^{\alpha} \zeta_{ij}^{\alpha}(\mathbf{x}) (\zeta_{ij}^{\alpha}(\mathbf{x}'))^* \quad (3)$$

The quantity  $\Gamma$  is a Hermitian, positive-semidefinite matrix whose eigenvectors are rank ordered conduction paths according to their conjugate eigenvalue.<sup>[43]</sup> The quantity  $g_{ij}$  is defined as<sup>[43]</sup>

$$g_{ij}(\mathbf{k}, \omega) = \frac{2\pi e^2}{3m^2 \omega \Omega} [f_i(\mathbf{k}) - f_j(\mathbf{k})] \delta(\varepsilon_j(\mathbf{k}) - \varepsilon_i(\mathbf{k}) - \hbar\omega) \quad (4)$$

where  $\Omega$  is the cell volume, and  $f$  is the Fermi–Dirac distribution.  $\zeta_{ij}^{\alpha}(\mathbf{x}) \equiv \psi_i^{\dagger}(\mathbf{x}) p^{\alpha} \psi_j(\mathbf{x})$  is a complex-valued function,  $\psi_i(\mathbf{x})$  is the  $i$ th Kohn–Sham eigenfunction, and  $p^{\alpha} = \frac{\hbar}{i} \frac{\partial}{\partial x_{\alpha}}$ , ( $\alpha = x, y, z$ ). We have used this approach to successfully describe transport in a solid electrolyte material,<sup>[43]</sup> Cu-doped  $\alpha$ -alumina,<sup>[44]</sup> and Cu-doped tantala.<sup>[45]</sup>

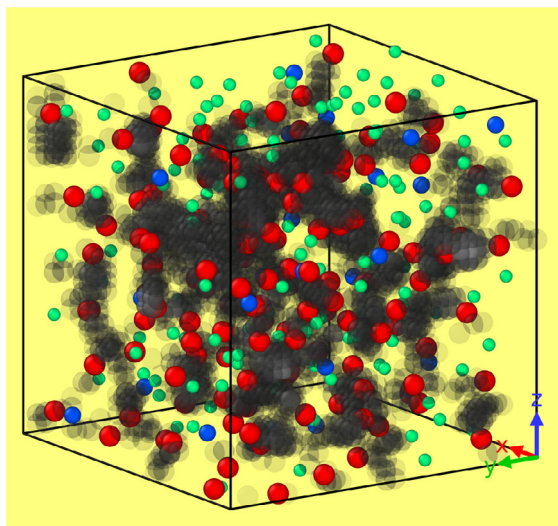


**Figure 7.** SPC for FEAR-I shown in grayscale. The Zr sites have higher SPC values than the Cu sites, and Al seems almost irrelevant to conduction.

The SPC for FEAR-I model is visualized as a grayscale plot in **Figure 7**. The SPC is distributed on both Cu and Zr, but a close analysis reveals that the Zr atoms have higher SPC values than the Cu atoms in the network.

### 3.4. Vibrational Properties

FEAR-II was well relaxed with the lattice vectors being allowed to change to attain zero pressure. This produces a slightly non-orthogonal supercell and an overall volume change of 45%. Each atom was displaced in six directions ( $\pm x$ ,  $\pm y$ ,  $\pm z$ ) by ( $\approx 0.015$  Å), and after each of these small displacements, forces were computed on all atoms, to obtain the force constant matrix and dynamical matrix. Normal modes were computed from the dynamical matrix by direct diagonalization. The vibrational density of states (VDoS) is defined as

$$g(\omega) = \frac{1}{3N} \sum_{i=1}^{3N} \delta(\omega - \omega_i) \quad (5)$$

with  $N$  and  $\omega_i$  representing the number of atoms and the eigenfrequencies of normal modes, respectively. The elemental contribution to the VDoS was computed with species projected VDoS defined as<sup>[46]</sup>

$$g_{\alpha}(\omega) = \frac{1}{3N} \sum_{i=1}^{N_{\alpha}} \sum_n |e_i^n|^2 \delta(\omega - \omega_n) \quad (6)$$

$|e_i^n|^2$  are the eigenvectors of the normal modes, and  $N_{\alpha}$  is the total number of atoms of  $\alpha$  species.

As shown in **Figure 8**, the VDoS is peaked at  $\approx 125$   $\text{cm}^{-1}$  arising from a joint contribution of vibrations of heavier atoms (Cu, Zr), whereas Al only contributes to vibrations at higher end of the vibrational spectrum. The partial VDoS plot supports these findings.

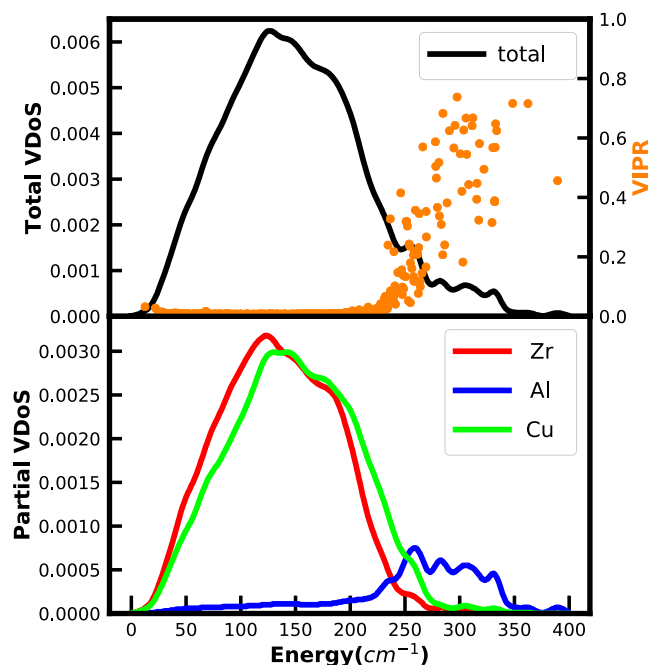


**Figure 8.** Total vibrational DoS for the FEAR-II model (top panel). The total vibrational localization (VIPR), shown by orange dots, shows that low-frequency modes are extended, whereas those at high frequencies are localized. Species projected VDoS (bottom panel) shows high-frequency modes dominated by the lightest atom and low frequency by heavier atoms, as expected.

#### 3.4.1. Localization of Vibrational Modes

The localization of vibrational modes is not easily observable from experiments. To study the localization of vibrational modes, we calculate the vibrational IPR (VIPR), the vibrational analogue of the electronic IPR, from the eigenvectors as follows

$$\mathcal{V}(\omega_n) = \frac{\sum_{i=1}^N |\mathbf{u}_n^i|^4}{(\sum_{i=1}^N |\mathbf{u}_n^i|^2)^2} \quad (7)$$

where  $(\mathbf{u}_n^i)$  is the displacement vector of  $i$ th atom at normal mode frequency  $\omega_n$ .

A small value of VIPR for a particular eigenfrequency indicates evenly distributed vibration among the atoms, whereas a higher value implies vibration localized on few atoms. We have plotted the total VIPR in **Figure 8**. Low values of VIPR below  $\approx 250$   $\text{cm}^{-1}$  suggest extended/localized vibrational modes at low frequencies. However, above  $250$   $\text{cm}^{-1}$ , we observe higher VIPR and localized vibrations.

To gain a visual insight into the localization/delocalization of vibrations, suitable animations were made. The higher frequency animation shows that Al atoms exhibit local motion (both bond stretching and bending) like that of a rattler inside a cage of Cu, Zr atoms. Similar, rattler motion of light atoms inside a cage of metal atoms has been seen previously in a Pd-Ni-P BMG.<sup>[27]</sup>

## 4. Conclusion

We have generated realistic models of a complex BMG with FEAR that agrees reasonably well with the experiment. Both FEAR models have the same level of agreement with the experiment and topologically similar to the MQ model (all ab initio roads lead to  $\text{Cu}_{46}\text{Zr}_{46}\text{Al}_8$ ). However, the computational efficiency of the FEAR model was almost six times that of the MQ model. A similar efficiency increase was reported earlier for Pd–Ni–P BMG.<sup>[27]</sup> The Voronoi statistics agree well with previous results, and our models may well be suited to catch the local dynamics of the clusters in the material. The addition of Al introduces structural clusters that are believed to have slow dynamics, thereby enhancing the GFA. We have also shown the temperature dependence of the distribution of some important Voronoi clusters and achieved reasonable agreement with published results. The electronic DoS of our models is very close to that of  $\text{Cu}_{50}\text{Zr}_{50}$ ,<sup>[40]</sup> suggesting that 8% Al concentration is not enough to significantly change the electronic properties.

## Acknowledgements

The authors thank the National Science Foundation (NSF) for support under DMR award 1507670. They also thank Extreme Science and Engineering Discovery Environment (XSEDE), supported by NSF grant number ACI-1548562, for providing computation resources under the allocations DMR-190008P.

## Conflict of Interest

The authors declare no conflict of interest.

## Keywords

forced enhanced atomic refinement, glass forming ability, space-projected conductivity

Received: July 27, 2020

Revised: November 20, 2020

Published online:

- [1] V. Kumar, T. Fujita, K. Konno, M. Matsuura, M. W. Chen, A. Inoue, Y. Kawazoe, *Phys. Rev. B* **2011**, *84*, 134204.
- [2] H. Li, Y. Zheng, *Acta Biomater.* **2016**, *36*, 1.
- [3] J. D. Bernal, *Nature* **1960**, *185*, 68.
- [4] P. H. Gaskell, *Nature* **1978**, *276*, 484.
- [5] D. Miracle, *Nat. Mater.* **2004**, *3*, 697.
- [6] P. Guan, T. Fujita, A. Hirata, Y. Liu, M. W. Chen, *Phys. Rev. Lett.* **2012**, *108*, 175501.
- [7] A. Takeuchi, A. Inoue, *Mater. Trans.* **2005**, *46*, 2817.
- [8] T. R. Anantharaman, C. Suryanarayana, *J. Mater. Sci.* **1971**, *6*, 1111.
- [9] K. Georgarakis, A. R. Yavari, D. V. Louzguine-Luzgin, J. Antonowicz, M. Stoica, Y. Li, M. Satta, A. LeMoulec, G. Vaughan, A. Inoue, *Appl. Phys. Lett.* **2009**, *94*, 191912.
- [10] J. Antonowicz, A. Pietnoczka, W. Zalewski, R. Bacewicz, M. Stoica, K. Georgarakis, A. Yavari, *J. Alloys Compd.* **2011**, *509*, S34.
- [11] L. Yang, G.-Q. Guo, L.-Y. Chen, S.-H. Wei, J.-Z. Jiang, X.-D. Wang, *Scr. Mater.* **2010**, *63*, 879.
- [12] X. Wang, Q. Jiang, Q. Cao, J. Bednarcik, H. Franz, J. Jiang, *J. Appl. Phys.* **2008**, *104*, 093519.
- [13] X. K. Xi, M. T. Sandor, H. J. Wang, J. Q. Wang, W. H. Wang, Y. Wu, *J. Phys.: Condens. Matter* **2011**, *23*, 115501.
- [14] Y. Q. Cheng, E. Ma, H. W. Sheng, *Phys. Rev. Lett.* **2009**, *102*, 245501.
- [15] V. Kokotin, H. Hermann, J. Eckert, *J. Phys.: Condens. Matter* **2011**, *23*, 425403.
- [16] Y. Zhang, N. Mattern, J. Eckert, *J. Alloys Compd.* **2012**, *514*, 141.
- [17] P. Yu, H. Bai, M. Tang, W. Wang, *J. Non-Cryst. Solids* **2005**, *357*, 1328.
- [18] I. Kaban, P. Jovari, B. Escher, D. Tran, G. Svensson, M. Webb, T. Regier, V. Kokotin, B. Beuneu, T. Gemming, J. Eckert, *Acta Mater.* **2015**, *100*, 369.
- [19] D. A. Drabold, *Eur. Phys. J. B* **2009**, *68*, 1.
- [20] A. Pandey, P. Biswas, D. A. Drabold, *Sci. Rep.* **2016**, *6*, 33731.
- [21] A. Pandey, P. Biswas, D. A. Drabold, *Phys. Rev. B* **2015**, *92*, 155205.
- [22] A. Pandey, P. Biswas, B. Bhattarai, D. A. Drabold, *Phys. Rev. B* **2016**, *94*, 235208.
- [23] B. Bhattarai, A. Pandey, D. Drabold, *Carbon* **2018**, *131*, 168.
- [24] D. Igram, B. Bhattarai, P. Biswas, D. Drabold, *J. Non-Cryst. Solids* **2018**, *492*, 27.
- [25] Q. Zhou, T. Du, L. Guo, M. Smedskjaer, M. Bauchy, *J. Non-Cryst. Solids* **2020**, *536*, 120006.
- [26] B. Bhattarai, P. Biswas, R. Atta-Fynn, D. A. Drabold, *Phys. Chem. Chem. Phys.* **2018**, *20*, 29.
- [27] B. Bhattarai, R. Thapa, D. A. Drabold, *Modell. Simul. Mater. Sci. Eng.* **2019**, *27*, 075002.
- [28] M. G. Tucker, D. A. Keen, M. T. Dove, A. L. Goodwin, Q. Hui, *J. Phys.: Condens. Matter* **2007**, *19*, 335218.
- [29] G. Kresse, J. Furthmuller, *Phys. Rev. B* **1996**, *54*, 11169.
- [30] M. Hacene, A. Anciaux-Sedrakian, X. Rozanska, D. Klahr, T. Guignon, P. Fleurat-Lessard, *J. Comput. Chem.* **2012**, *33*, 2581.
- [31] M. Hutchinson, M. Widom, *Comput. Phys. Commun.* **2012**, *183*, 1422.
- [32] P. E. Blochl, *Phys. Rev. B* **1994**, *50*, 17953.
- [33] G. Kresse, D. Joubert, *Phys. Rev. B* **1999**, *59*, 1758.
- [34] J. P. Perdew, K. Burke, M. Ernzerhof, *Phys. Rev. Lett.* **1996**, *77*, 3865.
- [35] A. Stukowski, *Simul. Modelling, Mater. Sci. Eng.* **2010**, *18*, 015012.
- [36] E. A. Lazar, J. Han, D. J. Srolovitz, *Proc. Natl. Acad. Sci. USA* **2015**, *112*, E5769.
- [37] S. Q. Wu, C. Z. Wang, S. G. Hao, Z. Z. Zhu, K. M. Ho, *Appl. Phys. Lett.* **2010**, *97*, 021901.
- [38] S. G. Hao, C. Z. Wang, M. J. Kramer, K. M. Ho, *J. Appl. Phys.* **2010**, *107*, 053511.
- [39] U. Mizutani, Y. Yamada, C. Mishima, T. Matsuda, *Solid State Commun.* **1987**, *62*, 641.
- [40] J. Antonowicz, A. Pietnoczka, K. Pkaa, J. Latuch, G. A. Evangelakis, *J. Appl. Phys.* **2014**, *115*, 203714.
- [41] R. Kubo, *J. Phys. Soc. Jpn.* **1957**, *12*, 570.
- [42] D. A. Greenwood, *Proc. Phys. Soc.* **1958**, *71*, 585.
- [43] K. Prasai, K. N. Subedi, K. Ferris, P. Biswas, D. A. Drabold, *Phys. Status Solidi RRL* **2018**, *12*, 1800238.
- [44] K. N. Subedi, K. Prasai, M. N. Kozicki, D. A. Drabold, *Phys. Rev. Mater.* **2019**, *3*, 065605.
- [45] R. Thapa, B. Bhattarai, M. N. Kozicki, K. N. Subedi, D. A. Drabold, *Phys. Rev. Mater.* **2020**, *4*, 064603.
- [46] A. Pasquarello, J. Sarnthein, R. Car, *Phys. Rev. B* **1998**, *57*, 22.